Microimaging of Oxygen Concentration near Live Photosynthetic Cells by Electron Spin Resonance

Revital Halevy,[†] Victor Tormyshev,[‡] and Aharon Blank[†*]
[†]Schulich Faculty of Chemistry Technion, Israel Institute of Technology, Haifa, Israel; and [‡]Novosibirsk Institute of Organic Chemistry, and Novosibirsk State University, Novosibirsk, Russia

ABSTRACT We present what is, to our knowledge, a new methodology for high-resolution three-dimensional imaging of oxygen concentration near live cells. The cells are placed in the buffer solution of a stable paramagnetic probe, and electron spin-resonance microimaging is employed to map out the probe's spin-spin relaxation time (T_2). This information is directly linked to the concentration of the oxygen molecule. The method is demonstrated with a test sample and with a small amount of live photosynthetic cells (cyanobacteria), under conditions of darkness and light. Spatial resolution of ~30 × 30 × 100 μm is demonstrated, with ~μM oxygen concentration sensitivity and sub-fmol absolute oxygen sensitivity per voxel. The use of electron spin-resonance microimaging for oxygen mapping near cells complements the currently available techniques based on microelectrodes or fluorescence/phosphorescence. Furthermore, with the proper paramagnetic probe, it will also be readily applicable for intracellular oxygen microimaging, a capability which other methods find very difficult to achieve.

INTRODUCTION

Oxygen is one of the most important molecules in the cycle of life. It serves as the terminal electron acceptor of oxidative phosphorylation in the mitochondria and is used in the production of reactive oxygen species. The measurement of oxygen is important for the study of phenomena such as mitochondrial and metabolic functions, signaling pathways, stimuli effects, membrane permeability, and disease differentiation (1–4). Oxygen consumption is, therefore, an informative marker of cellular metabolism applicable to a broad array of biological systems, from the mitochondria to cells to whole organisms. Due to its importance, many methods have been developed for the measurement of oxygen in live systems. For example, magnetic resonance imaging can be used noninvasively to obtain a qualitative estimation of oxygen levels with millimeter-scale resolution (5,6). Electrochemical microelectrodes can measure, accurately, the oxygen levels in tissues and around cells in an invasive manner at a specific location with spatial resolution down to the scale of a few microns (7,8). A variety of fluorescence- and phosphorescence-based methods can be used to estimate the oxygen levels in individual cells (9–12). Last but not least, electron spin resonance (ESR) can be used to obtain accurate measurements of oxygen concentration in tissues and cells (4,13,14). In fact, this last method is considered (not only by ESR experts) to be the gold standard for intracellular oxygen quantification (15,16), and at least equivalent to electrochemical methods for extracellular applications.

Despite this wide array of methodologies, there are still many gaps in the field of oxygen sensing both for large samples at low resolution and, especially, for small samples at high resolution. For example, in applications that require high-resolution (in the micrometer scale) three-dimensional oxygen imaging of a sample containing a single or a few cells, there is really no reasonable methodology in existence that can cope with this challenge. To the best of our knowledge, there are only a few examples in the literature of experiments that actually try to provide high-resolution oxygen maps of live cells. All of them involve the use of optical methods employing several types of fluorescent or phosphorescent probes, and their results are not sufficient in accuracy, precision, and/or resolution (9,11,12,15,17–20).

The main problem with the optical-based methods is that they rely on measurements of fluorescence or phosphorescence lifetimes for the estimation of oxygen concentration. These times depend heavily on microenvironmental parameters as well as additional bioactive molecules found both inside and outside the cells. This makes the absolute calibration very difficult, and results in significant variation among the results (9). Moreover, these limitations, along with some naturally occurring fluorescent or phosphorescent signal from the sample, result in increased noise in the lifetime measurements that may lead to the erroneous estimation of oxygen concentration, even in homogenous synthetic devices (21).

Further to that, there are other acute issues that limit the use of optical-based methods employing soluble probes. These include problems of photostability of the exogenous probes, lack of simple and efficient means of delivery into the cell, requirements for minimal cytotoxicity, nonoptimal photophysical properties, and problems of operational performance in conditions of a typical live-cell imaging experiment. Some of these limitations may be solved by the use of synthesized micron- and submicron-sized particulate probes containing photostable dyes. However, the absolute accuracy and precision problems are still evident in the experimental measurements based on such kinds of probes

Submitted March 1, 2010, and accepted for publication May 3, 2010.

*Correspondence: ab359@tx.technion.ac.il

Editor: David D. Thomas.

© 2010 by the Biophysical Society

0006-3495/10/08/0971/8 $2.00

doi: 10.1016/j.bpj.2010.05.002

(10,12). In addition, loading via micron-size projectile delivery or endocytosis is rather inefficient and may cause irreparable damage to the cell, while random distribution of the small number of particulate sensors within the cell may give a poor representation of intracellular oxygen distribution.

As mentioned above, ESR is considered to be a gold standard in the assessment of oxygen concentration in biosystems (16). ESR-based methods employ a variety of exogenous paramagnetic probes (either soluble or solid nanocrystal particulates) that are added to the sample, in a manner similar to optical probes (22). The soluble paramagnetic oxygen molecule at concentration $[O_2]$ interacts with the ESR paramagnetic probe that shortens its spin-spin relaxation time, T_2, according to the expression (23)

$$\frac{1}{T_2(C,D)} = \frac{1}{T_2^0(C,D)} + k(C,D)[O_2]. \quad (1)$$

Here, $T_2{}^0$ is the spin-spin relaxation time of the probe under anoxic conditions (depending on the probe's concentration, C, and its diffusion coefficient, D), and k is a proportionality constant. In most cases the diffusion coefficient does not vary much for live samples (although, if needed, it can, in principle, be directly evaluated also by ESR (24,25)), and the spin concentration is obtained during the imaging process. Therefore, this relation can be used to directly measure the oxygen concentration and thus makes ESR oxymetry a widely applicable and accurate method, mainly for in vivo applications in small animals (4,16,26,27). It should be noted that, in principle, NMR could also be used to make direct measurements of local oxygen concentration by measuring the oxygen-sensitive T_1 relaxation rate of perfluorocarbon-based exogenous probes (28). However, NMR is much less sensitive and thus cannot be used for microscopic applications.

ESR can measure and image oxygen concentration in live specimens very well, but up until now it has been employed mainly on relatively large samples with low (millimeter-scale) image resolution. Recently, we have made substantial progress in the field of induction detection ESR microimaging (ESRM) (29–31). This new methodology is basically a scaled-down version of common magnetic resonance imaging systems, aiming at the observation of millimeter- and submillimeter-sized samples with micron to deep submicron image resolution. Achieving such resolution requires a very high spin sensitivity of at least 10^6–10^7 electron spins, together with the capability to produce strong magnetic field gradient pulses of ~100 T/m for a duration of ~1 μs or less (24,31). When using solid test samples, ESRM has recently been able to achieve a spatial resolution slightly better than 1 μm (31).

Here we show, for the first time to our knowledge, how ESRM can be applied to the high-resolution three-dimensional imaging of oxygen concentration near live species (cyanobacteria cells). This new capability can replace the cumbersome point measurements made with oxygen electrodes currently used in these types of applications (8). Furthermore, in the near future, it may also be used for high-resolution intracellular oxygen mapping—a capability that other modalities find very difficult to achieve.

MATERIALS AND METHODS

Materials

The perdeuterated "Finland" trityl radical was synthesized at Novosibirsk using the method described in Talmon et al. (25). The BG-11 buffer was prepared according to the protocol detailed in Rippka et al. (32). The cyanobacteria used in this work are cyanobacterium *Synechocystis sp*. PCC 6803.

ESR microscopy system

The ESR microimaging system used in this work was described in detail in Blank et al. (31) and the referenced documents therein. In brief, it is a home-made pulsed system operating at ~17 GHz and equipped with a miniature and sensitive imaging probe. At room temperature it demonstrated spin sensitivity of ~3 × 10^6 spins (for an acquisition time of ~1 h and samples with a linewidth of ~0.1 G) and an image resolution slightly better than 1 μm (for a high-spin concentration sample with ~10^8 spins per [1 μm]^3). For this work we have added the capability to illuminate the sample using an optical fiber 1 mm in diameter, with a measured light intensity of ~25 W/m^2. In addition, we used a water-saturated temperature-controlled air flow into the imaging probe to maintain a constant temperature of 25°C during the live-sample imaging experiments and prevent fast sample dehydration.

The experiments described here employed the pulse sequence shown in Fig. 1, which is essentially a conventional Hahn echo imaging pulse sequence, using magnetic field phase gradients in the X and Y axes and a frequency encoding gradient along the Z axis (30,31). With this method, the ESR echo signal of the entire sample is recorded for different sets of X and Y phase gradients, while the Z gradient is kept constant. This process results in many ESR echo signal vectors being recorded in the time domain for all given combinations of X and Y phase gradients. The acquired data can then be arranged in a three-dimensional matrix containing these time domain

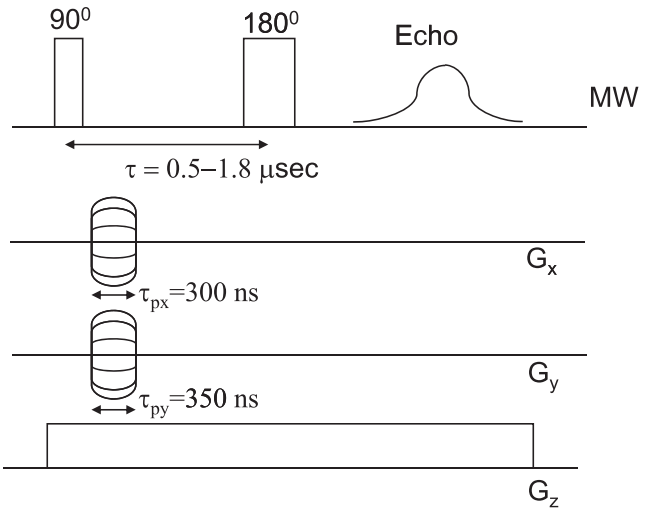

FIGURE 1 Typical ESR pulse sequence used for microimaging. A simple Hahn echo with a pulse separation of τ, two phase gradients in the X and Y axes with durations of τ_{px} and τ_{py}, respectively, and a constant gradient along the Z axis.

vectors for all X- and Y-phase gradient combinations. A three-dimensional Fourier transform process performed on this matrix provides the three-dimensional image of the spatial distribution of the ESR signal. Hanning's window apodization is usually applied during the Fourier transform process, with no zero filling. The typical resolution for a liquid radical solution near live specimens can be ~10–30 μm (depending on the imaging time, radical concentration, and required signal/noise ratio), with typical field of view of 1–2 mm in all three spatial axes. Several ESR images, collected with different interpulse delay τ (see Fig. 1), enable the extraction of the spatially resolved relaxation time T_2. This is carried out by analyzing the data from all images for each voxel, which analysis exhibits a decay in the signal as τ is stepped up. This signal decay (as a function of τ) can be characterized for each voxel by fitting it into an exponential decay function with two parameters: voxel amplitude signal (proportional to the number of spins in each voxel) and the decay time constant (T_2) (31). Specific experimental parameters (pulse sequence timings and delays, gradients, and imaging times) are described in the relevant paragraph of Results.

Sample preparation

Solutions of 1 mM of trityl in water/glycerol mixtures (glycerol percentage of 20%, 35%, 50%, and 60%) were prepared and sealed in capillary glass tubes under vacuum after several freeze-pump-thaw cycles. A 3-mM solution of trityl in BG-11 buffer was also prepared and sealed in capillary tubes under vacuum in the same manner. The test sample with the trityl solution in different water/glycerol mixtures was prepared by taking the solution from the above-mentioned capillary tubes and placing it in a specially prepared glass sample holder divided into four quadrants. (Details of the photolithography process are provided in Halevy et al. (33).) The depth of each quadrant is ~100 μm. A slight amount of paraffin oil was added to the trityl solutions in the four-quadrant sample to minimize condensation and dehydration. The entire process of test sample preparation and sealing was carried out in a glove box under Ar atmosphere.

For the preparation of the live-cells sample, a few squares of absorbent paper with a size of ~400 × 400 μm were inserted into an Eppendorf tube which was then filled with 1.2 mL of the cyanobacterium suspension (concentration of 40 mg/mL). The suspension was centrifuged for 2 min at 6000 RPM. After this, the supernatant buffer was completely removed except for ~50 μL, which were left to avoid cyanobacteria dehydration. As a result of this process, the absorbent paper was now saturated by the cyanobacteria. A few fibers were then extracted from the paper by tweezers and were placed on the bottom of a cuplike sample holder, with 3 mM of trityl in BG-11 solution, and then sealed, leaving a small air outlet open (see Fig. 2). The trityl concentration in the sample after dilution by the wet paper is ~1.25 mM (estimated based on its signal magnitude and relaxation time). The number of cells in the test tube as a result of this procedure was estimated using a flow cytometer (LSR-II Analyzer; Becton-Dickinson, Franklin Lakes, NJ) to be ~600,000 cells. This corresponds to a dry weight mass of ~0.75 μg in our sample for typical cyanobacteria cells (34).

T_2 measurements

The reference measurements of T_2 were carried out using the samples placed in the sealed capillary tubes (described later in Oxygen Concentration Near Live Cyanobacteria) apart from the one with normal atmosphere. The tubes were inserted into the dielectric resonator in the imaging probe from the top and a Hahn echo sequence was used for T_2 measurements.

Numerical calculation of oxygen distribution in the sample holder

The numerical analysis of the expected oxygen distribution inside our sample holder with the oxygen-producing photosynthetic species was carried out with the aid of COMSOL Multiphysics (using Ver. 3.5, and the Chemical Engineering Diffusion Module; COMSOL, Burlington, MA). The dimensions of our sample holder were included in the simulation (see Fig. 2 and later, Fig. 5) with insulating boundary conditions in all sides except for a small air outlet with atmospheric oxygen concentration boundary conditions. Other parameters used in the simulation were:

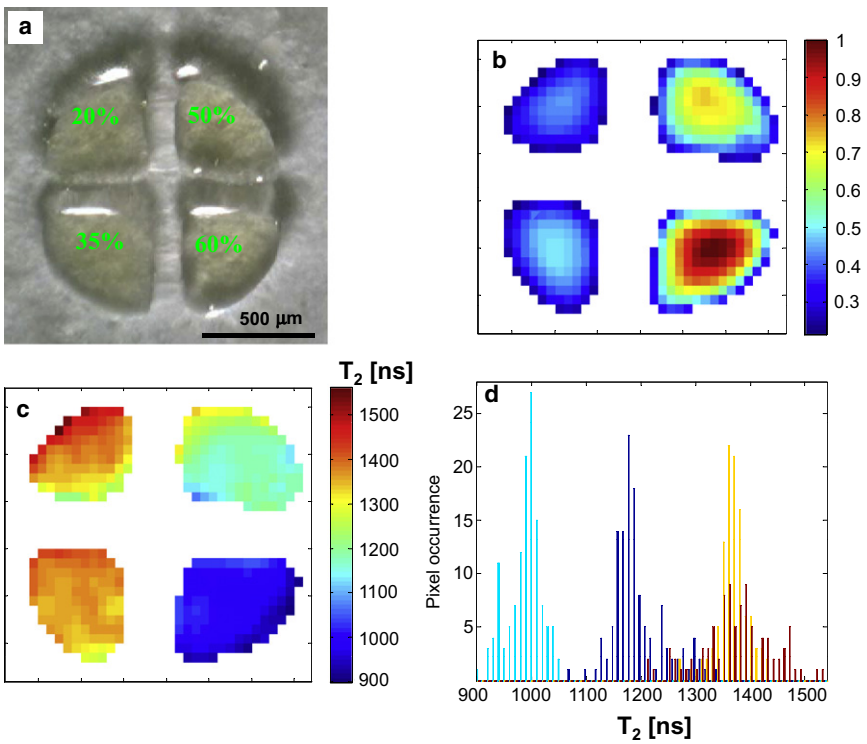

FIGURE 2 Images of the test sample. (*a*) Optical photo, showing the liquid sample in the four quadrants. The numbers mark the percentage of glycerol in water for each quadrant. (*b*) Amplitude ESR image (normalized). (*c*) Image of the fitted T_2. (*d*) Histogram of the fitted T_2 values for the four different quadrants. The resolution of the ESR images is ~30 × 30 μm.

Size of the O_2 production region: 0.4 × 0.4 × 0.15 mm (the box inside the tube in Fig. 5).
Diffusion constant of O_2 in the buffer: 2.19×10^{-5} m^2/s.
Diffusion constant of O_2 in air: 1.97×10^{-9} m^2/s.
O_2 concentration in air: 9.35 mol/m^3.
O_2 production rate: 0.0072 $mol \cdot m^{-3} \cdot s^{-1}$.
O_2 concentration in the buffer under normal atmosphere: 0.255 $mol \cdot m^{-3}$.

RESULTS

Test sample measurements

As noted above, the concentration of oxygen is proportional to $1/T_2$ of the paramagnetic probe employed. Therefore, the first issue to be addressed is ESRM's capability to map, accurately, T_2 values in test samples mimicking the conditions near live species (i.e., in aqueous environment). The paramagnetic probe used in this work is a water-soluble deuterated ''Finland'' trityl radical (25,35). We took advantage of the fact that T_2 of the trityl radical under anoxic conditions is dependent upon the solvent's viscosity (36,37). Thus, a test sample was prepared with 1-mM solution of trityl in four different water/glycerol mixtures (20%, 35%, 50%, and 60% of glycerol in water), each characterized by a different viscosity (38) (~1.97, 3.82, 8.63, and 17.45 cP at 20°C). The T_2 values of these mixtures (under anoxic conditions; see Materials and Methods) were measured by our pulsed ESR system using a two-pulse Hahn echo experiment, and were found to be 3782 ± 80, 2158 ± 43, 1396 ± 16, and 1013 ± 14 ns for the 20% up to the 60% glycerol/water solutions, respectively. After this stage, a test sample made of the four trityl solutions was prepared.

The solutions were placed in a special photolithographically prepared glass sample holder in the shape of a circle divided into four quadrants (refer to Materials and Methods). The sample was imaged using the imaging pulse sequence shown in Fig. 1, but without any gradient along the Z axis (pure two-dimensional image) (30,31). The ESR imaging results of the test sample are shown in Fig. 2. Six images with different values of delay (τ = 500, 600, 800, 1000, 1400, and 1800 ns) between the 90° and 180° microwave pulses were acquired. The data from the six images was analyzed for each pixel to obtain a match to an exponential decay function with two parameters: pixel amplitude signal (proportional to the number of spins in each pixel) and the decay time constant (T_2) (31). Areas with low signal/noise ratio, located outside and in between the quadrants (i.e., with no trityl solution), were discarded (*white color*).

In principle, every quadrant should have exhibited a single T_2 value. In practice, noise and image artifacts resulted in a distribution of T_2 values, as shown in Fig. 2 *d*. The values of T_2 obtained here (1373 ± 69, 1365 ± 28, 1195 ± 46, and 988 ± 31, for the 20% up to the 60% glycerol/water solutions, respectively) were lower than the ones measured for the sealed capillary tubes. This is due to the difficulty in preparing such sample (see Materials and Methods) without dehydration and under complete anoxic conditions. Nevertheless, it still served its purpose of evaluating the distribution of T_2 values and thus enabled an assessment of the quality of our measurements. The spread in the results is mainly due to random effects of noise, systematic errors related to slight pixel movements, and resolution changes between the images taken at different τ-values. The wider spread of results in the low-viscosity quadrant (20%) is probably caused by the dehydration of the thin layer of solvent employed (~50 μm). Based on the results of Fig. 2, one can conclude that the accuracy of T_2 mapping is ~3% for the T_2 values that are relevant for oxygen measurements in and near live systems (see below).

Calibration of the $[O_2]$ vs. $1/T_2$ ratio

As noted in the Introduction, it is known that for a given viscosity (i.e., given spin probe diffusion coefficient) and spin concentration values, the value of $1/T_2$ is proportional to the concentration of oxygen. The live sample images are all taken under normal water viscosity. Thus, to translate the T_2 data in the live samples' ESR microimages to oxygen concentration data, one must first find the proportionality factor between $1/T_2$ and the oxygen concentration at a variety of radical concentration values. This is achieved by measuring the T_2 values (using a Hahn echo sequence) under anoxic and normal atmospheric conditions, for a 1.25-mM trityl in BG-11 buffer solution, which was the radical concentration used during the live-samples imaging study. The measured values of $T_2^{atm} = 468 \pm 10$ ns and $T_2^0 = 2186 \pm 20$ ns correspond to oxygen concentrations of ~255 μM and ~0. The atmospheric oxygen concentration value assumed here is characteristic of a solution of ~1.25 mM of salt in water at 25°C (39,40). These two values were used in our analysis of the oxygen concentration based on the T_2 measurements. A simple application of Eq. 1 provided the value of $k = 6.55 \times 10^{-6}$ [1/(ns × μM)].

Oxygen concentration near live cyanobacteria

After these preliminary experiments, a set of measurements were conducted for several samples of cyanobacteria cells placed in our special glass sample holders (shown in Fig. 3, *a* and *b*; see also Materials and Methods). Fig. 3 *c* shows a picture of one of the samples we measured. Fig. 4 presents typical results obtained for this sample by the ESRM imaging experiments, under dark and light conditions (i.e., without and with direct light illumination into the imaging probe; see Materials and Methods). Table 1 summarizes the quantitative results of Fig. 4. The amplitude and T_2 data were extracted from three three-dimensional ESR images obtained by Hahn echo imaging pulse sequences with τ-values of 500, 600, and 700 ns. The acquisition time for each image was ~5 min (composed of <1 min for a single-scan image acquisition, and then it was repeated

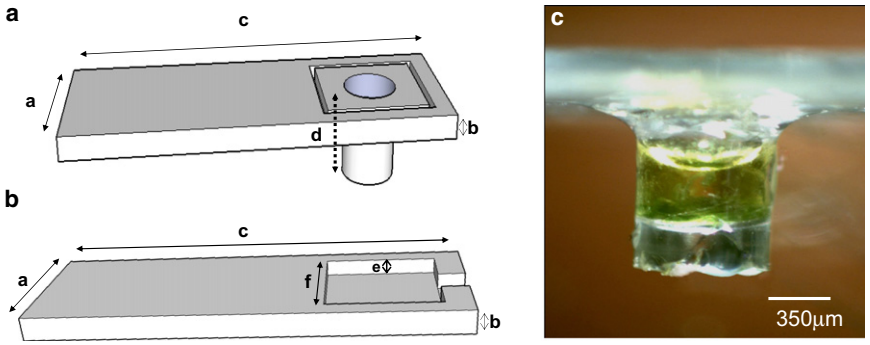

FIGURE 3 The live cells sample of cyanobacteria in trityl solution. (*a*) Schematic drawing of the glass sample holder, prepared using photolithography. Typical dimensions of the sample holder are: $a = 3.8$ mm, $b = 250$ μm, $c = 22$ mm, and $d = 1.6$ mm. (*b*) Schematic drawing of the matching glass cover used to seal the sample, apart from a small air outlet. Typical dimensions for the cover are: $e = 100$ μm, $f = 2$ mm. (*c*) Optical photo of a typical sample after preparation (shown from the side). The cyanobacteria are at the bottom while the trityl solution is around and above them.

for the acquisition of six scans for signal-averaging purposes).

Referring to the imaging pulse sequence shown in Fig. 1, the 90° and 180° pulse durations were 50 and 90 ns, respectively. The pulsed gradient durations were 300 and 350 ns with peak amplitudes of 4.1 and 3 *T*/m for the *X* and *Y* gradients, respectively. These values correspond to an image resolution of ~30 μm in the *XY* plane (31). The constant *Z*-gradient amplitude was 0.8 *T*/m, leading to a resolution of ~35 μm (assuming a nominal T_2 of 400 ns (31)). The resolution figures were verified in our previous work with similar experimental systems, employing well-defined solid test samples (30,31). To improve sensitivity, slices ~100-μm-thick in the Z dimension were considered in the analysis of the results. The results of the amplitude images (Fig. 4, *a–c*) show that most of the cyanobacteria were located on the right side of the tube, leading to smaller signals from that region. The $T_2/[O_2]$ images taken under dark conditions exhibit similar values for all three *Z* slices, both within the slices and from slice to slice, as expected. When the light is turned on, a significant overall reduction in T_2 (i.e., increase in $[O_2]$) is observed. Furthermore, a significant gradient of oxygen along the *Z* axis is apparent (variation of $[O_2]$ from slice to slice), while smaller gradients and $[O_2]$ inhomogeneities in the *XY* plane are also observed. As in the case of the test sample, slight changes in the images taken at different τ-values lead to edge artifacts where the sample tube ends.

DISCUSSION

The imaging results in Fig. 4 show for the first time, to our knowledge, an experimental capability to map oxygen concentrations three-dimensionally in a micrometer-scale

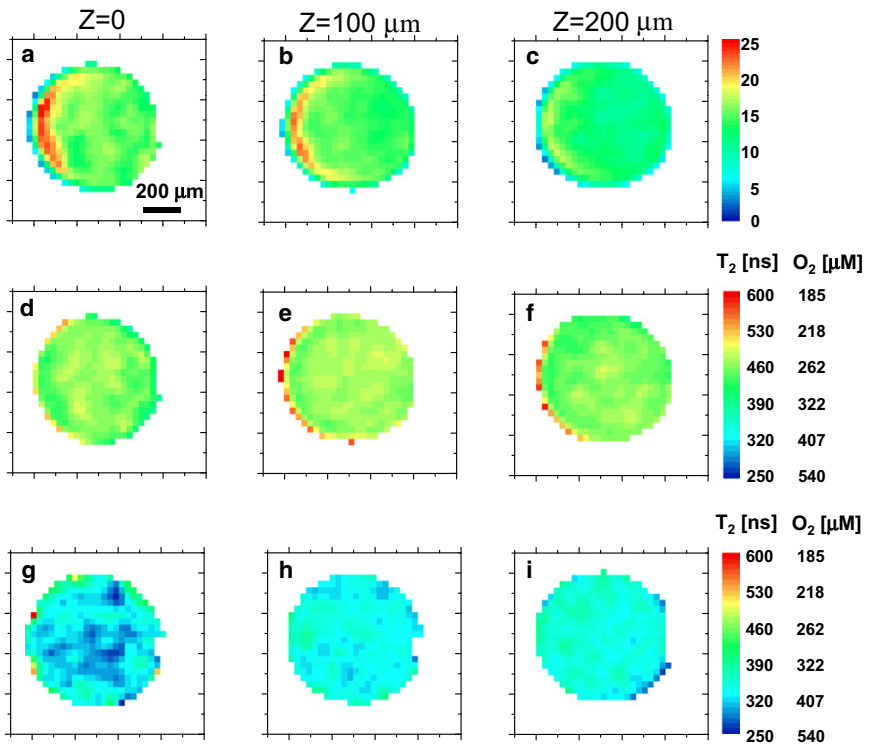

FIGURE 4 ESR microimages of the live cells sample. The first row (plates *a–c*) shows the amplitude images at three different *Z* slices, as extracted from the raw ESR images. The second row (plates *d–f*) shows the T_2 (and the corresponding $[O_2]$) images for the same three *Z* slices under dark conditions. The third row (plates *g–i*) shows the T_2 (and the corresponding $[O_2]$) images for the same three *Z* slices under light conditions. Note that all plates in the first column correspond to location $Z = 0$ along the sample tube, while the second and third columns correspond to $Z = 100$ and 200 μm, respectively.

TABLE 1 Summary of the ESR microimaging results for the live-cells sample shown in Fig. 4

Slice position [μm]	T_2 [ns]	O_2 [μM]
Z = 0, 100, 200 (light off)	470 ± 18	255 ± 10
Z = 0 (light on)	329 ± 24	394 ± 34
Z = 100 (light on)	342 ± 16	376 ± 18
Z = 200 (light on)	352 ± 18	364 ± 22

The numbers represent the mean and standard deviation results for each slice. The data representing the dark condition has a relatively small spread, both in-plane and between slices. The data for the light condition shows pronounced differences with respect to the dark condition and also considerable gradients of O_2 from slice to slice. The in-plane variations are also quite large under light conditions, especially in the lower slice where most of the cyanobacteria are located.

resolution near live cellular species. Such types of measurements can be interpreted using analytical or numerical models to evaluate the oxygen generation/consumption rate of the species under various conditions and stimuli. This can be carried out by adapting Fick's law of diffusion to the specific measurement setup in an open sample (8) or by simply looking at overall oxygen consumption/production with the cells placed in a small closed compartment (41). Our present work involved an open compartment, but can, in principle, also be used in closed spaces. An example of a calculation procedure that is relevant to the current experimental setup is given in Fig. 5. Here we show the results of a simple numerical model for calculating the oxygen concentration generated by a photosynthetic oxygen production mass (with boxlike shape) inside our sample holder (see Materials and Methods for calculation details). The calculation is carried out with a single fitting parameter, which is the oxygen production rate, found to be ~38 μg of oxygen (per μg of dry weight) per hour. The experimental results of Fig. 4 (summarized in Table 1) show good agreement with this theoretical analysis: The oxygen gradient values in the *XY* plane are rather small both in theory and in the actual experiment, while the gradient along the *Z* axis is much larger and readily apparent in the experimental data. Independent verification of the oxygen gradients with an oxygen microelectrode was not possible in this case, due to the use of a cover slide, which blocks the electrode's access. Still, one can compare our results to those appearing in the literature and show similar levels of variation in oxygen concentration as a function of the distance from an oxygen source in a sample open to air in a steady state (8) (with proper scaling of the size of the oxygen-generating source).

As for the absolute value of the oxygen production rate per dry weight, this can be compared to previous literature references that mention values of ~75 μg (μg of dry weight)$^{-1}$ h^{-1} (for the cyanobacterium *Oscillatoria agardhii* (42), at the given light irradiation power; see Materials and Methods), and ~176 μg (μg of dry weight)$^{-1}$ h^{-1} (for the cyanobacterium *Synechocystis sp*. PCC 6803 that was used in this work, at optimal conditions (43,44)). These figures are larger than the ones we obtained in our work. This is probably due to nonoptimal light irradiation and temperature conditions. Furthermore, the increased oxygen concentration in the small sample holder possibly tends to suppress the oxygen production rate. The intention of our work was mainly to show a capability to acquire high-resolution three-dimensional oxygen images rather than providing exact numbers for the oxygen production rate. The limited accuracy in estimating the number of cells in the sample and the possible uneven light irradiation conditions within the sample prevent us from providing here accurate oxygen production rates per cell. However, in the future, on the basis of our current setup (and anticipating an even better setup), we feel that oxygen production/consumption rates per cell using a closed sample containing very few cells or large single cells (such as *Foraminifera*) in a partly open sample could be accurately evaluated.

The measurements performed on the four-quadrant test sample and the live species lead to the conclusion that, around atmospheric pressure, the current oxygen concentration sensitivity is at ~10 μM (~4% accuracy), and with the

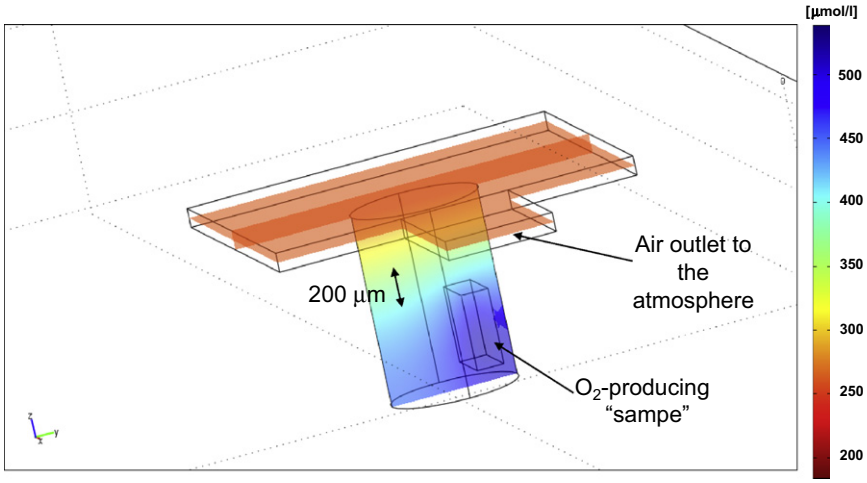

FIGURE 5 Numerical calculation of the oxygen concentration in our sample holder due to oxygen-producing mass located at the bottom. The results are the steady-state solution that is reached after 5 min. The 200-μm scale arrow represents approximately the volume covered by the experimental images for the Z = 0-, 100-, and 200-μm slices.

atmospheric pressure at ~1/10 of (i.e., typical hypoxic/intracellular conditions), the oxygen concentration sensitivity is ~3.5 μM (~14% accuracy). These figures translate into an absolute oxygen sensitivity of ~0.9 and ~0.31 fmol in a single voxel (with a size of ~30 $\times$ 30 $\times$ 100 μm), under atmospheric and hypoxic conditions, respectively. The level of T_2 noise, which limits oxygen concentration sensitivity as well as the resolution and imaging time, can be further improved using higher magnetic fields (e.g., ~1.2 T corresponding to a microwave frequency of ~35 GHz, where an imaging probe has already been constructed and tested). In this field, a smaller probe with shorter gradient pulses and higher spin sensitivity would enable a spatial resolution of ~5 μm with imaging time of a few minutes (employing the trityl water soluble spin probes) (45). The shorter gradient pulses (~100 ns) to be used with the small probe would enable us to minimize image artifacts and reduce the minimal echo separation, τ—thereby further improving sensitivity.

A methodological tool for the three-dimensional mapping of oxygen in the micrometer scale near live cells can be useful for many applications. For example, it can be used as part of a single-cell metabolic rate monitoring system with fmol/minute resolution, capable of observing many cells at the same time, which constitutes an important goal in life-science research (41).

Another example of the use of ESRM for oxygen concentration monitoring is the possible observation of oxygen gradients in complex multicellular systems such as cancer spheroids, under various stimuli and genetic manipulations (46) (replacing the invasive microelectrode methods). Finally, the great hope is that ESRM would enable, with the aid of intracellular probes, to map, accurately, the oxygen inside moderately-sized cells. Solid nanoscale intracellular probes are already available (22), but they are not suitable for pulsed ESRM, and we still need to wait for the appearance of solid probes with longer T_2 (these are currently being developed). Further to that, esterified derivatives of the water-soluble trityl spin probe show good promise for intracellular measurements; we plan to experiment with these new materials in the future (47).

We thank Prof. Noam Adir and Faris Salame from the Schulich Faculty of Chemistry at the Technion for their help regarding the supply and handling of the cyanobacteria. The help and support of Svetlana Yoffis from the Technion Micro-Nano Fabrication Unit is also greatly appreciated.

This work was partially supported by grant No. 213/09 from the Israeli Science Foundation, grant No. 2005258 from the Binational Science Foundation, grant No. 201665 from the European Research Council, and the Russell Berrie Nanotechnology Institute.

REFERENCES

1. Xi, Q., S. Y. Cheranov, and J. H. Jaggar. 2005. Mitochondria-derived reactive oxygen species dilate cerebral arteries by activating Ca^{2+} sparks. *Circ. Res.* 97:354–362.
2. Simpkins, C., S. Balderman, and E. Mensah. 1998. Mitochondrial oxygen consumption is synergistically inhibited by metallothionein and calcium. *J. Surg. Res.* 80:16–21.
3. Swartz, H. M. 2004. Using EPR to measure a critical but often unmeasured component of oxidative damage. *Oxygen. Antioxid. Redox Signal.* 6:677–686.
4. Swartz, H. M., N. Khan, …, T. Walczak. 2004. Clinical applications of EPR: overview and perspectives. *NMR Biomed.* 17:335–351.
5. Mancini, D. M., J. R. Wilson, …, J. S. Leigh. 1994. In vivo magnetic resonance spectroscopy measurement of deoxymyoglobin during exercise in patients with heart failure. Demonstration of abnormal muscle metabolism despite adequate oxygenation. *Circulation.* 90:500–508.
6. Prasad, P. V., R. R. Edelman, and F. H. Epstein. 1996. Noninvasive evaluation of intrarenal oxygenation with BOLD MRI. *Circulation.* 94:3271–3275.
7. Evans, S. M., K. D. Judy, …, C. J. Koch. 2004. Comparative measurements of hypoxia in human brain tumors using needle electrodes and EF5 binding. *Cancer Res.* 64:1886–1892.
8. Land, S. C., D. M. Porterfield, …, P. J. Smith. 1999. The self-referencing oxygen-selective microelectrode: detection of transmembrane oxygen flux from single cells. *J. Exp. Biol.* 202:211–218.
9. Zhong, W., P. Urayama, and M. A. Mycek. 2003. Imaging fluorescence lifetime modulation of a ruthenium-based dye in living cells: the potential for oxygen sensing. *J. Phys. D.* 36:1689–1695.
10. Koo, Y. E. L., Y. F. Cao, …, M. A. Philbert. 2004. Real-time measurements of dissolved oxygen inside live cells by organically modified silicate fluorescent nanosensors. *Anal. Chem.* 76:2498–2505.
11. Zhang, G. Q., G. M. Palmer, …, C. L. Fraser. 2009. A dual-emissive-materials design concept enables tumor hypoxia imaging. *Nat. Mater.* 8:747–751.
12. Finikova, O. S., A. Y. Lebedev, …, S. A. Vinogradov. 2008. Oxygen microscopy by two-photon-excited phosphorescence. *ChemPhysChem.* 9:1673–1679.
13. Liu, K. J., P. Gast, …, H. M. Swartz. 1993. Lithium phthalocyanine: a probe for electron paramagnetic resonance oximetry in viable biological systems. *Proc. Natl. Acad. Sci. USA.* 90:5438–5442.
14. Pandian, R. P., and P. Kuppusamy. 2004. Lithiated phthalocyanines: a new class of crystalline paramagnetic probes for targeted cellular oximetry and imaging by EPR spectroscopy. *Biophys. J.* 86:191a.
15. Sud, D., and M. A. Mycek. 2009. Calibration and validation of an optical sensor for intracellular oxygen measurements. *J. Biomed. Opt.* 14:020506.
16. Swartz, H. M. 2002. Measuring real levels of oxygen in vivo: opportunities and challenges. *Biochem. Soc. Trans.* 30:248–252.
17. Kuhl, M., G. Holst, …, P. J. Ralph. 2008. Imaging of oxygen dynamics within the endolithic algal community of the massive coral *Porites lobata*. *J. Phycol.* 44:541–550.
18. Dunphy, I., S. A. Vinogradov, and D. F. Wilson. 2002. Oxyphor R2 and G2: phosphors for measuring oxygen by oxygen-dependent quenching of phosphorescence. *Anal. Biochem.* 310:191–198.
19. Gerritsen, H. C., and C. J. de Grauw. 2000. Fluorescence lifetime imaging of oxygen in dental biofilm. *SPIE Proc.* 4164:70–78.
20. Takahashi, E., K. Sato, …, K. Doi. 1998. Direct observation of radial intracellular PO^{-2} gradients in a single cardiomyocyte of the rat. *Am. J. Physiol. Heart Circ. Physiol.* 44:H225–H233.
21. Sud, D., G. Mehta, …, M. A. Mycek. 2006. Optical imaging in microfluidic bioreactors enables oxygen monitoring for continuous cell culture. *J. Biomed. Opt.* 11:050504.
22. Kutala, V. K., N. L. Parinandi, …, P. Kuppusamy. 2004. Simultaneous measurement of oxygenation in intracellular and extracellular compartments of lung microvascular endothelial cells. *Antioxid. Redox Signal.* 6:597–603.
23. Zweier, J. L., and P. Kuppusamy. 1994. In vivo EPR spectroscopy of free radicals in the heart. *Environ. Health Perspect.* 102 (*Suppl 10*): 45–51.

24. Blank, A., Y. Talmon, …, W. Harneit. 2008. Direct measurement of diffusion in liquid phase by electron spin resonance. *Chem. Phys. Lett.* 465:147–152.

25. Talmon, Y., L. Shtirberg, …, A. Blank. 2010. Molecular diffusion in porous media by PGSE ESR. *Phys. Chem. Chem. Phys.* 12:5998–6007.

26. He, G. L., A. Samouilov, …, J. L. Zweier. 2002. In vivo imaging of free radicals: applications from mouse to man. *Mol. Cell. Biochem.* 234-235:359–367.

27. Springett, R., and H. M. Swartz. 2007. Measurements of oxygen in vivo: overview and perspectives on methods to measure oxygen within cells and tissues. *Antioxid. Redox Signal.* 9:1295–1301.

28. Peschke, P., S. Hunjan, …, P. Peschke. 2003. Tumor oximetry: comparison of F-19 MR EPI and electrodes. *Oxygen Transp. Tissue XXIV.* 530:19–27.

29. Blank, A., C. R. Dunnam, …, J. H. Freed. 2003. High resolution electron spin resonance microscopy. *J. Magn. Reson.* 165:116–127.

30. Blank, A., C. R. Dunnam, …, J. H. Freed. 2004. Pulsed three-dimensional electron spin resonance microscopy. *Appl. Phys. Lett.* 85:5430–5432.

31. Blank, A., E. Suhovoy, …, W. Harneit. 2009. ESR imaging in solid phase down to sub-micron resolution: methodology and applications. *Phys. Chem. Chem. Phys.* 11:6689–6699.

32. Rippka, R., J. Deruelles, …, R. Y. Stanier. 1979. Generic assignments, strain histories and properties of pure cultures of cyanobacteria. *J. Gen. Microbiol.* 111:1–61.

33. Halevy, R., Y. Talmon, and A. Blank. 2007. Photolithographic production of glass sample holders for improved sensitivity and resolution in ESR microscopy. *Appl. Magn. Reson.* 31:591–598.

34. Mahlmann, D. M., J. Jahnke, and P. Loosen. 2008. Rapid determination of the dry weight of single, living cyanobacterial cells using the Mach-Zehnder double-beam interference microscope. *Eur. J. Phycol.* 43:355–364.

35. Ardenkjaer-Larsen, J. H., I. Laursen, …, K. Golman. 1998. EPR and DNP properties of certain novel single electron contrast agents intended for oximetric imaging. *J. Magn. Reson.* 133:1–12.

36. Yong, L., J. Harbridge, …, H. J. Halpern. 2001. Electron spin relaxation of triarylmethyl radicals in fluid solution. *J. Magn. Reson.* 152: 156–161.

37. Owenius, R., G. R. Eaton, and S. S. Eaton. 2005. Frequency (250 MHz to 9.2 GHz) and viscosity dependence of electron spin relaxation of triarylmethyl radicals at room temperature. *J. Magn. Reson.* 172: 168–175.

38. Shankar, P. N., and M. Kumar. 1994. Experimental determination of the kinematic viscosity of glycerol water mixtures. *Proc. Roy. Soc. London Ser. A Math. Phys. Eng. Sci.* 444:573–581.

39. Carpenter, J. H. 1966. New measurements of oxygen solubility in pure and natural water. *Limnol. Oceanogr.* 11:264–277.

40. Garcia, H. E., and L. I. Gordon. 1992. Oxygen solubility in seawater—better fitting equations. *Limnol. Oceanogr.* 37:1307–1312.

41. Molter, T. W., M. R. Holl, …, D. R. Meldrum. 2008. A new approach for measuring single-cell oxygen consumption rates. *IEEE Trans. Autom. Sci. Eng.* 5:32–42.

42. Post, A. F., J. G. Loogman, and L. R. Mur. 1986. Photosynthesis, carbon flows and growth of *Oscillatoria-agardhii Gomont* in environments with a periodic supply of light. *J. Gen. Microbiol.* 132: 2129–2136.

43. Tang, X. S., D. A. Chisholm, …, B. A. Diner. 1993. Spectroscopic evidence from site-directed mutants of *Synechocystis* PCC6803 in favor of a close interaction between histidine 189 and redox-active tyrosine 160, both of polypeptide D2 of the photosystem II reaction center. *Biochemistry.* 32:13742–13748.

44. Schledz, M., A. Seidler, …, G. Neuhaus. 2001. A novel phytyltransferase from *Synechocystis sp.* PCC 6803 involved in tocopherol biosynthesis. *FEBS Lett.* 499:15–20.

45. Blank, A., and J. H. Freed. 2006. ESR microscopy and nanoscopy with ''induction'' detection. *Isr. J. Chem.* 46:423–438.

46. Bjerkvig, R. 1992. Spheroid Culture in Cancer Research. CRC Press, Boca Raton, FL.

47. Liu, Y. P., F. A. Villamena, …, J. L. Zweier. 2009. Esterified trityl radicals as intracellular oxygen probes. *Free Radic. Biol. Med.* 46:876–883.